iScience

CellPress
OPEN ACCESS

Article

Tuning transport in graphene oxide membrane with single-site copper (II) cations

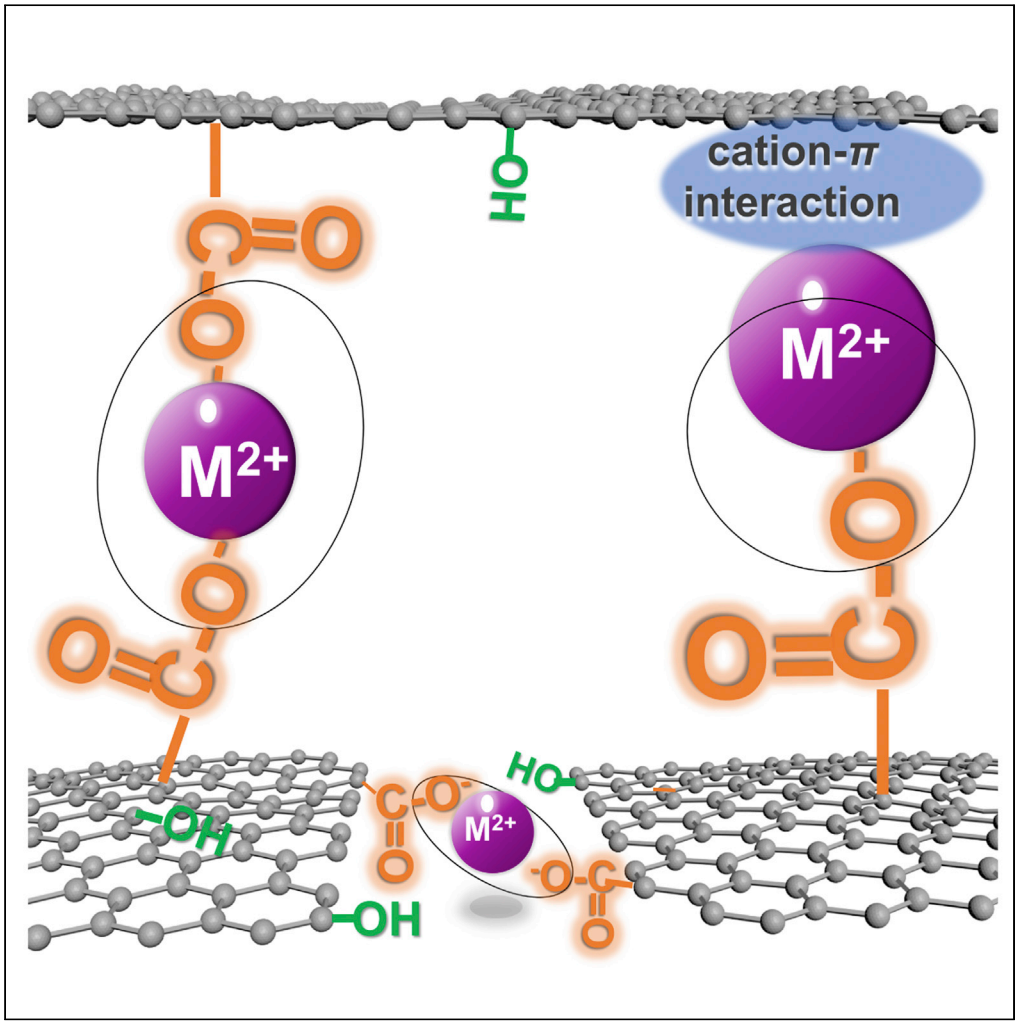

Mingzhan Wang, Xiang He, Eli Hoenig, ..., David M. Tiede, Hua Zhou, Chong Liu

chongliu@uchicago.edu

Highlights

Single-site Cu^{2+} decreases the interlayer spacing of wet graphene oxide membrane

Single-site Cu^{2+} modifications can enhance salt rejection

Wang et al., iScience 25, 104044
April 15, 2022
https://doi.org/10.1016/j.isci.2022.104044

iScience

CellPress
OPEN ACCESS

Article

Tuning transport in graphene oxide membrane with single-site copper (II) cations

Mingzhan Wang,[1] Xiang He,[2] Eli Hoenig,[1] Gangbin Yan,[1] Guiming Peng,[1] Fengyuan Shi,[3] Julia Radhakrishnan,[1] Grant Hill,[1] David M. Tiede,[2] Hua Zhou,[4] and Chong Liu[1,5,*]

SUMMARY

Controlling the ion transport through graphene oxide (GO) membrane is challenging, particularly in the aqueous environment due to its strong swelling tendency. Fine-tuning the interlayer spacing and chemistry is critical to create highly selective membranes. We investigate the effect of single-site divalent cations in tuning GO membrane properties. Competitive ionic permeation test indicates that Cu^{2+} cations dominate the transport through the 2D channels of GO membrane over other cations (Mg^{2+}/Ca^{2+}/Co^{2+}). Without/With the single-site M^{2+} modifications, pristine GO, Mg-GO, Ca-GO, and Cu-GO membranes show interlayer spacings of ~13.6, 15.6, 14.5, and 12.3 Å in wet state, respectively. The Cu-GO membrane shows a two-fold decrease of NaCl (1 M) permeation rate comparing to pristine GO, Mg-GO, and Ca-GO membranes. In reverse osmosis tests using 1000 ppm NaCl and Na_2SO_4 as feeds, Cu-GO membrane shows rejection of ~78% and ~94%, respectively, which are 5%–10% higher than its counterpart membranes.

INTRODUCTION

With the climate change and increasing global population, water scarcity is projected to be a more and more challenging problem (Shannon et al., 2008). Producing clean water from saline water (e.g. seawater) via desalination is highly desirable (Elimelech and Phillip, 2011; Werber et al., 2016). Owing to the high energy efficiency and economic viability, membrane-based reverse osmosis is among the most appealing desalination technologies, including distillation, direct solar steaming (Fang et al., 2013; Jia et al., 2017; Yang et al., 2019a; Zhao et al., 2018; Zhou et al., 2016), and membrane-based desalination (Humplik et al., 2011) (Park et al., 2017; Tan et al., 2018). Designing better membrane materials to achieve both high selectivity and high permeability will benefit the desalination energy efficiency as well as reduce the footprint of desalination plant.

Studies in the past decade have shown that carbon-based nanomaterials could be promising candidates to serve as high-performance reverse osmosis membrane (Huang et al., 2015; Sun et al., 2016). For example, aligned carbon nanotube forest membrane is demonstrated to have an ultrafast water transport while keeping a high salt rejection rate (Fornasiero et al., 2008; Holt et al., 2006). Recently, theoretical predictions and experimental results indicate that single-layer graphene with sub-nanoscale pores could achieve nearly complete salt rejection and water permeability several orders of magnitude higher than commercial polymer membrane (Cohen-Tanugi and Grossman, 2012; Surwade et al., 2015; Yang et al., 2019b). However, it is challenging to develop a scalable and convenient method to create robust single-layer graphene with uniform sub-nanoscale pores (O'Hern et al., 2015; Wang and Karnik, 2012). As an alternative, graphene oxide (GO) membrane with well-defined two-dimensional channels, can be readily fabricated in a scalable manner and is demonstrated to have high permeability to water (Nair et al., 2012) with a clear-cut size sieving effect for hydrated ions and small organic molecules (Joshi et al., 2014; Nie et al., 2020). Yet, GO suffers from significant swelling in its wet state due to the oxygen-rich functional groups on the surface. The resultant channel height, i.e. interlayer spacing of GO is typically above 1 nm in wet state, thus falling short of achieving efficient rejection to ions with small hydrated radius (Mi, 2019). Mechanical confinement (Abraham et al., 2017), controlled reduction (Zhang et al., 2018), chemical spacers (Chen et al., 2017; Jia et al., 2016; Morelos-Gomez et al., 2017; Thebo et al., 2018) *etc.* have been investigated to inhibit the swelling of GO membrane in its wet state. Interestingly, potassium ion (K^+)-treated GO membranes are reported to be capable of rejecting ions efficiently in the H-cell trans-membrane permeation test,

[1]Pritzker School of Molecular Engineering, University of Chicago, Chicago, IL 60637, USA

[2]Advanced Materials for Energy-Water Systems (AMEWS) Energy Frontier Research Center and Chemical Sciences and Engineering Division, Argonne National Laboratory, Lemont, IL 60439, USA

[3]Electron Microscopy Core, University of Illinois Chicago, Chicago, IL 60607, USA

[4]X-Ray Science Division, Advanced Photon Source, Argonne National Laboratory, Lemont, IL 60439, USA

[5]Lead contact

*Correspondence: chongliu@uchicago.edu

https://doi.org/10.1016/j.isci.2022.104044

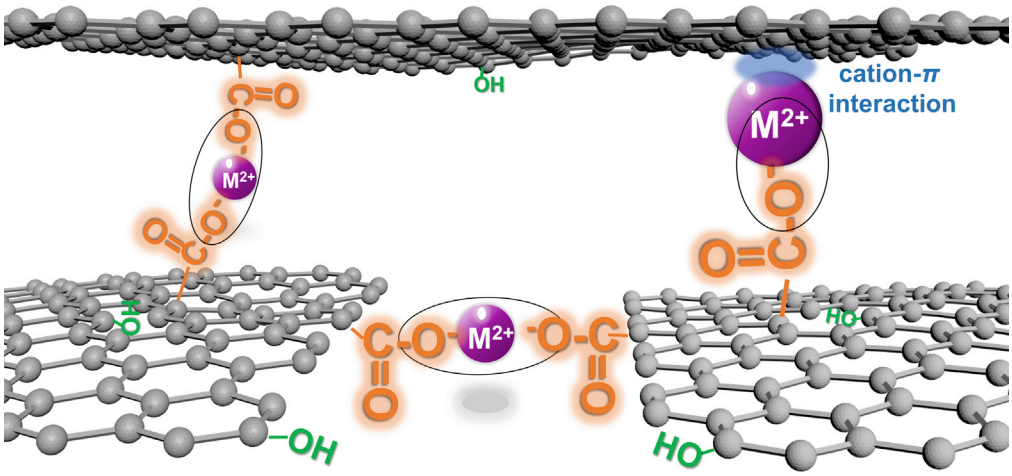

Figure 1. Schematic illustration of the possible interactions between divalent metal cations and graphene oxide matrices

For clarity, only the predominant hydroxyl and carboxyl group are presented in GO sheet and their ratios are not commensurate with the real sample used. M^{2+} represents divalent metal cation.

presumably due to the resultant fixed interlayer spacing of GO membrane (Chen et al., 2017). Similar result is also reported for the Al^{3+}-treated MXene membranes (Ding et al., 2020).

Structurally, it is generally accepted that GO is composed of intact graphene patches and oxygen-rich functional groups, like hydroxyl, carboxyl, carbonyl *etc.*(Dreyer et al., 2010) When considering the interactions between metal cations and GO matrices, besides the well-known electrostatic interactions between metal ions and carboxylate group, the cation-π interactions also play an important role (Liu et al., 2015; Mahadevi and Sastry, 2013; Sun et al., 2014), as schematically illustrated in Figure 1. Compared with monovalent potassium ion, metal cations with higher valence can have stronger interactions with GO. The case should be more prominent for transition metal cations particularly, where the presence of *d* orbital electrons will lead to much richer chemistry there.

Here, we investigated the interactions of divalent ions to GO membrane and their roles in controlling the mass transport through GO membranes. We discovered that Cu^{2+} dominated the transport across the GO membranes with the presence of equal molarity of Mg^{2+} and Ca^{2+}. When used as spacers, Cu^{2+} could decrease the interlayer spacing of GO in the wet state from 13.6 Å to 12.3 Å. However, Ca^{2+} and Mg^{2+} enlarged the interlayer spacing of GO membranes to 15.6 Å and 14.5 Å, respectively. Trans-membrane permeation tests showed that the GO membrane with Cu^{2+} decoration decreased the permeability to salt (1M NaCl) to half as compared to pristine GO membrane. The reverse osmosis tests also verified that with Cu^{2+} decoration, the GO membrane could enhance the rejection rates of 1000 ppm and 2000 ppm NaCl feed solution from ~70% to ~78% and from ~60% to ~69%, respectively. By contrast, Ca^{2+} and Mg^{2+} decorations did not show obvious effect to GO membranes in both the trans-membrane permeation tests and reverse osmosis tests. Our results coherently point to the exotic role of Cu^{2+} in tuning the interlayer chemistry of graphene oxide.

RESULTS AND DISCUSSION

Competitive permeation test of divalent cations across GO membrane

Well-dispersed GO colloidal solution was used as the precursor for membrane fabrication (Figure S1). Pristine GO membrane was made by filtering GO solution onto a porous and nonselective PTFE support under the assistance of vacuum. See Transparent Method section in the supplemental information for detailed membrane fabrication procedure. Scanning electron microscopy (SEM) images showed that the as-prepared GO membrane was a uniform film with a topology fluctuation translated from the underlying PTFE support (Figure S2). The thickness of GO membrane for tests is ~120 nm (dry state, 0.5 mg loading) unless noted otherwise.

First, we performed the competitive permeation test of M^{2+} cations across GO membrane, which was mounted in between the two chambers of H-type cell, as schematically illustrated in Figure 2A. 20 mL of

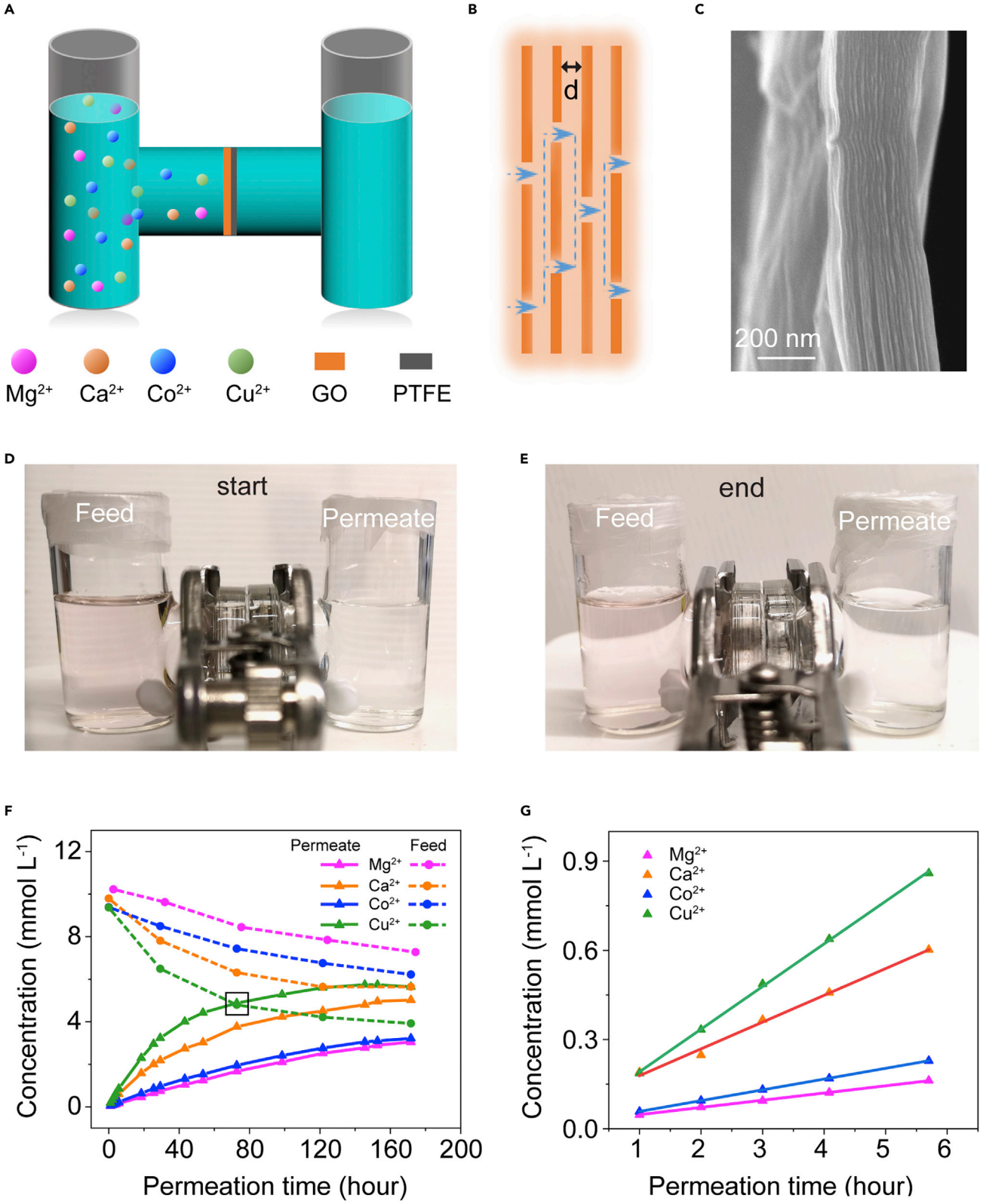
A
B
C
d
200 nm
Mg2+
Ca2+
Co2+
Cu2+
GO
PTFE
D
start
Feed
Permeate
E
end
Feed
Permeate
F
Permeate
Feed
Mg2+
Ca2+
Co2+
Cu2+
Concentration (mmol L-1)
Permeation time (hour)
G
Mg2+
Ca2+
Co2+
Cu2+
Concentration (mmol L-1)
Permeation time (hour)

Figure 2. Competitive trans-membrane permeation test of M^{2+} cations with equal molarity across GO membrane

(A) Schematic of the trans-membrane permeation test in an H-type cell. Chloride anion (Cl^-) is omitted in the schematic for clarity.

(B) Schematic of the mass transport pathways in the two-dimensional channels within GO membrane.

(C) Cross-sectional SEM image of GO membrane (mass loading 1 mg) showing a well-defined layered structure.

(D and E) Photos showing the start and the end of the competitive trans-membrane permeation test setup, respectively.

(F) Time-dependent cationic concentrations in the permeate side. The rectangle box highlights the concentration profile crossover of Cu^{2+} between the feed and permeate.

(G) Linear fitting of the cationic concentration profiles of the permeate chamber in the initial permeation stage.

the mixture solution of $MgCl_2/CaCl_2/CoCl_2/CuCl_2$ with equal molarity (~10 mM, pH ~4.7) was added into the feed chamber, while 20 mL of deionized water was added into the permeate chamber. Co^{2+} and Cu^{2+} are chosen as the representatives of transitional metal ions, given their stability and strong bindings with carboxylate group. Both chambers were stirred vigorously to mitigate the concentration polarization. Driven by the concentration gradient, the ions would diffuse from the feed to permeate, across the tortuous two-dimensional channels within GO membranes (Figures 2B and 2C), and water molecules would be reversely transported across GO membranes simultaneously to balance the osmosis pressure between the feed and permeate. Figures 2D and 2E show the photos of the start and the end of the permeation test, respectively. The initial mixture solution of $MgCl_2/CaCl_2/CoCl_2/CuCl_2$ with equal molarity takes a pink color originating from the hexaaqua Co^{2+} ions $[Co(H_2O)_6]^{2+}$ (Figure 2D). During and at the end of the test, the solution in the feed chamber was still pink while that in the permeate chamber was nearly colorless (Figure 2E). Besides, a level difference ~3 mm was developed between the feed chamber and the permeate chamber due to osmosis. Both the developed level difference and color difference are reliable testaments to the integrity of the tested GO membrane and definitely point to the distinguishable transport rates of M^{2+} metal ions across the two-dimensional channels in GO membrane.

To quantify the trans-membrane transport rates of M^{2+} metal ions, we traced the cationic concentration changes in both the feed chamber and permeate chamber by ICP-MS. The result is shown in Figure 2F. Clearly, the concentrations of all the metal cations in permeate increased with time elapsing and tended to reach a stable value at the final stage, indicating the tendency toward the thermodynamics equilibrium between the feed and the permeate (see the detailed discussion in Figure S3). At the end of permeation test, the concentrations of $Mg^{2+}/Ca^{2+}/Co^{2+}/Cu^{2+}$ in the permeate and in the feed were 3.05/5.03/3.22/5.64 mM and 7.63/6.16/6.45/4.06 mM, respectively. At least, two striking points are noteworthy here. Firstly, the concentration of Cu^{2+} in the permeate is not only higher than those of other cations in the permeate but also higher than that of Cu^{2+} in the feed side since the middle of permeation test (from ~73 h as the rectangle box highlights in Figure 2F). By contrast, the concentration of $Mg^{2+}/Ca^{2+}/Co^{2+}$ in permeate is always lower than those in the feed side. The imbalanced distribution of the cations across the GO membrane is a reflection of their differences in the transmembrane transport speeds. The cross-over of Cu^{2+} can be explained by the tendency to achieve the global equilibrium across the membrane, which necessitates the collective motions of all the ions. Such imbalanced ion distribution might also suggest the establishment of Gibbs-Donnan potential across the membrane (Fievet, 2014). Secondly, by fitting the concentration data of permeate in the initial stage when the volume changes of permeate and the feed are negligible, the trans-membrane permeation rates of M^{2+} can be extracted by calculating the slopes (Figure 2G) (Joshi et al., 2014). The permeabilities of Mg^{2+}, Ca^{2+}, Co^{2+}, and Cu^{2+} are 120.8 ± 2.0, 448.0 ± 20.0, 180.3 ± 1.1, and 713.6 ± 10.0 mmol m^{-2} $hour^{-1}$, respectively. Interestingly, we find that the permeation rates of the ions do not simply follow the trend of their hydrated radii. The hydrated radii of Mg^{2+}, Ca^{2+}, Co^{2+}, and Cu^{2+} are 4.28, 4.12, 4.23, and 4.19 Å, respectively (Nightingale, 1959). On the other hand, the hydrated ions might undergo partly dehydration or deformation of the hydration shell to accommodate themselves into such confined two-dimensional nanochannels within GO membrane (Abraham et al., 2017; Chmiola et al., 2006). However, the fact that Cu^{2+} has the largest hydration enthalpy among the group should make it hardest to dehydrate or deform when passing through the confined two-dimensional nanochannels, thus pointing exactly to the contrary, *i.e.* the slowest permeation rate of Cu^{2+} (the hydration enthalpies of Mg^{2+}, Ca^{2+}, Co^{2+}, and Cu^{2+} are −1922, −1592, −2054, and −2,100 kJ/mol, respectively) (Burgess, 1978). Therefore, we attribute the counterintuitive fastest permeability of Cu^{2+} and imbalanced distribution of cations to the stronger interaction of Cu^{2+} cation with GO membrane comparing to other ions.

Besides our observation here, several evidence in the literatures can be invoked to support our conjecture here. First, Mg^{2+} or Ca^{2+} is free of whereas Cu^{2+} has *d* electrons, which play a central role in enabling coordination. The carboxyl groups can chelate with Cu^{2+} more tightly than Mg^{2+} and Ca^{2+}. Moreover, Tan

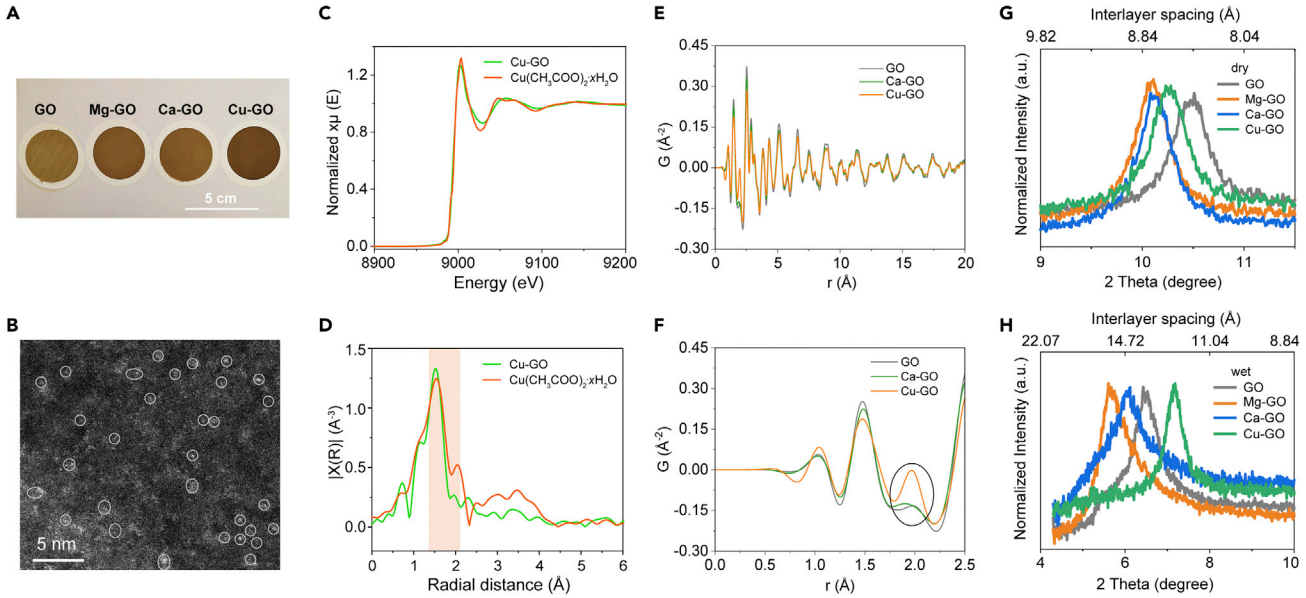

Figure 3. Characterization of M-GO membrane

(A) Photo of as-prepared GO-based membranes.

(B) HAADF-STEM image of Cu-GO. White cycles highlight some single-site Cu^{2+} in the membrane.

(C) XANES spectra of Cu K-edge.

(D) Fourier transformed EXAFS spectra of Cu K-edge in R space.

(E) PDFs of dry GO-based membranes. Note: Raw diffraction profiles and the corresponding reduced structure functions can be found in Figures S8 and S9.

(F) Close-up view of the plots in (E). The circle highlights the unique peak present in Cu-GO membrane.

(G and H) XRD patterns of GO-based dry and wet membranes, respectively.

et al. also reported that Cd^{2+} and Ni^{2+} in GO membrane could be displaced by Cu^{2+} (Tan et al., 2016). Recent theoretical calculations also show that Cu^{2+} has a much stronger adsorption energy on graphite with the cation-π interaction included (Shi et al., 2013).

Modification of GO membrane with single-site divalent cation (M-GO)

We then investigated the role of individual divalent ions in controlling the interlayer spacing of GO membranes. For the divalent metal cation-bridged GO membranes (denoted as M-GO), corresponding aqueous salt solution (0.01 M $MgCl_2$, $CaCl_2$, or $CuCl_2$ in water) was filtered through the as-prepared pristine GO membrane. See the Membrane fabrication section in the Method Details for detailed membrane modification procedures. SEM images of as-prepared membrane showed that there was no apparent morphological change after metal cation modifications (Figures S4A and S4B). We note that compared with the method of mixing of GO solution and salt solution together before membrane filtration (Mathesh et al., 2013; Sun et al., 2013; Wang et al., 2021), our modification method can avoid the aggregation or crumpling of GO flakes, thus guaranteeing the layered structure and the well-defined two-dimensional channels within the GO membrane (Figure S4C).

Notably, with the modifications of divalent cations, the colors of GO membranes turned darker visually (Figure 3A). UV-Vis spectra showed the enhanced absorption of GO membrane after the cation modifications nearly across the whole spectrum (Figure S5A). No obvious changes could be seen in the Raman spectra (Figure S5B). The stable concentrations of M^{2+} inside the GO membrane were measured by ICP-MS. As shown in Figure S6, the result showed Cu^{2+} had a decoration value of 2.21×10^{-7} mol per mg of GO (mol/mg_{GO}), higher than those of Mg^{2+} (0.43×10^{-7} mol/mg_{GO}) and Ca^{2+} (1.45×10^{-7} mol/mg_{GO}). The results could further support the conclusion drawn from the permeation test of M^{2+} in Figure 2, namely Cu^{2+} has stronger interactions with GO matrices. The high-angle annular dark-field scanning transmission electron microscope (HAAF-STEM) was used to identify the metal cations on GO. The images indicate that the divalent metal cations are populated randomly within GO membrane in the single-site form (Figures 3B and S7). Cu^{2+} showed higher decoration density in the GO membrane.

To gain more insights of the electronic and chemical environment of divalent metal ion in graphene oxide membrane, synchrotron-based X-ray absorption spectra of Cu-GO membrane were collected. The Cu K-edge X-ray absorption near-edge spectroscopy (XANES) confirms the copper ion remains divalent (Figure 3C). The extended X-ray fine structure (EXAFS) profiles in R space indicate that Cu species in GO shared similar characteristic coordination shells with copper (II) acetate hydrate (Figure 3D). The result suggests the strong interactions between Cu^{2+} and carboxylate group in GO, as schematically illustrated in Figure 1.

Further efforts were made to probe the atomic structures of the ion-decorated GO membranes using the pair distribution function (PDF) analysis of the total X-ray scattering profiles (Figures S8A and S9A). As shown in Figure S8B, the reduced structure functions of all dry GO membranes show strong and sharp Bragg peaks and broad diffuse features in low-Q and high-Q regions, respectively. In comparison, the reduced structure function of Ca-GO is very similar to that of the pristine dry GO membrane, while noticeable variation in the reduced structure function was found in the case of Cu-GO, suggesting the modified atomic structure of GO caused by the decoration of Cu^{2+}. After the Fourier transform of the reduced structure functions, real-space PDF patterns of the GO membranes are obtained and presented in Figure 3E. Overall, all the GO membranes present characteristic PDF patterns of graphene-based structures that are consistent with the previously reported data, (Woznica et al., 2015) which indicate that the decorations of metal ions do not damage the structural integrity of the parent GO membranes. Strikingly, one distinguishable atomic pair correlation at 1.97 Å that is absent in both dry GO and dry Ca-GO was found in the Cu-GO membrane (as circled out in Figure 3F), which should originate from the atomic pair distance between the decorated Cu^{2+} and the O in GO, once again corroborating the stronger interactions between the Cu^{2+} ions and the oxygen-rich functional groups on the GO surface, in good agreement with the EXAFS analysis mentioned above. The same PDF analyses were also carried out on the wet GO-based membranes (See Figure S9 for details), which show similar PDF patterns as the dry samples, implying the robustness of the atomic structure of GO in aqueous solutions. Of particular note, the wet Cu-GO membrane still exhibits a uniquely distinguished atomic pair correlation at 1.97 Å, confirming the stability of the decorated Cu^{2+} ions on GO membranes in the aqueous environments.

The interlayer spacings after M^{2+} decoration were measured using XRD. XRD patterns of as-prepared membranes in the dry state are shown in Figure 3G. The interlayer spacing of dry pristine GO membrane was *ca.* 8.4 angstrom (Å), while the interlayer spacings of dry GO membranes with the modification of all the three divalent cations become larger, *i.e.* Mg-GO (8.7 Å), Ca-GO (8.7 Å), and Cu-GO (8.6 Å). This is consistent with previous work reporting the enlarged interlayer spacings of GO membrane with Mg^{2+} and Ca^{2+} modification (Park et al., 2008). As mentioned before, GO membranes tend to swell in water, as shown in the XRD patterns (Figure 3H). However, M-GO membranes behave sharply contrasted when swollen in water. Similar to previous results (Chen et al., 2017), wet Mg-GO (15.6 Å) and Ca-GO (14.5 Å) membranes have larger interlayer spacings as compared with wet pristine GO (13.6 Å) membrane. But the Cu-GO membrane has a surprisingly suppressed interlayer spacing (12.3 Å) in the wet state. The result also indicates the superiority of our single Cu^{2+} cations modification method as opposed to previously reported Cu foil modification, which showed no decrease of interlayer spacing of wet GO membrane (Lv et al., 2020). A decreased interlayer spacing in the Cu-GO would benefit the membrane to have stronger repulsion to counter ions as well as better size sieving effect. Considering the thickness of GO sheet (~3.3 Å), the available space in the two-dimensional channels of the pristine GO, Mg-GO, and Ca-GO could accommodate approximately four to five layers of water in the wet state, while Cu-GO would accommodate approximately one layer less of water (Algara-Siller et al., 2015; Joshi et al., 2014; Ohkubo et al., 2018). As discussed in the former part, it is reasonable to infer that the strong interactions between Cu^{2+} and GO matrices render the inhibited swelling of and reduced water population within GO membrane. Like other cross-linked GO membrane (Jia et al., 2016; Lv et al., 2020; Park et al., 2008; Thebo et al., 2018; Yeh et al., 2015), we also observed the increased mechanical strength of M^{2+}-modified GO membranes when compared with unmodified GO membrane.

Forward and reverse osmosis tests of M-GO membranes

Encouraged by the different swelling behaviors of divalent metal cation-modified GO, we then examined their trans-membrane permeation rate to salt. The method is similar to the competitive transmembrane test in Figure 2A. Basically, different GO-based membranes to be tested were mounted in between the two chambers of H-type cell, and then 20 mL of 1 M NaCl aqueous solution and deionized water (DIW) were added into the separate chambers simultaneously, as schematically illustrated in Figure 4A. Both

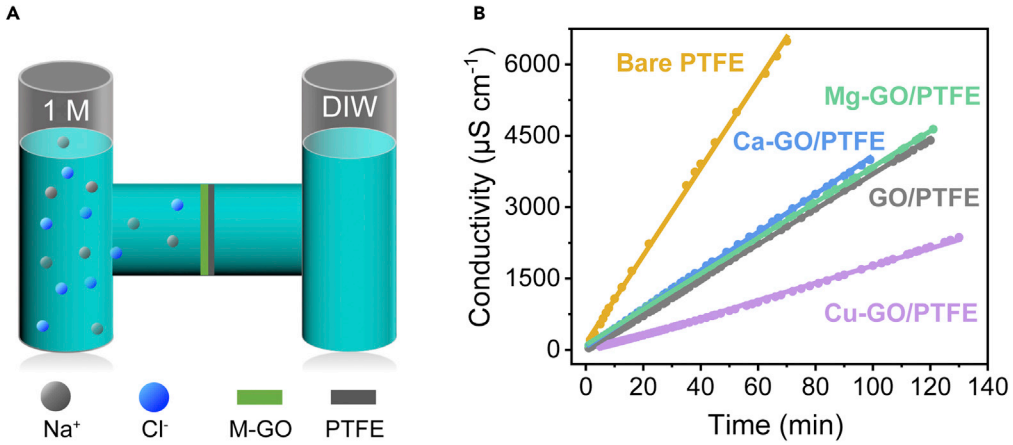

Figure 4. Trans-membrane permeation tests of NaCl across the GO-based membrane

(A) Schematic of the trans-membrane permeation rate test in an H-type cell.

(B) Time-dependent conductivity change of permeate.

chambers were stirred vigorously to mitigate the concentration polarization as well. The conductivity of permeate was continuously monitored. Linear increase of the conductivity on the DIW side was observed for all membranes tested (Figure 4B). The trans-membrane permeation rates were extracted by calculating the slopes (Joshi et al., 2014). The permeation rates of porous PTFE support, pristine GO/PTFE, Mg-GO/PTFE, Ca-GO/PTFE, and Cu-GO/PTFE membranes are 12.79 ± 0.10, 5.16 ± 0.08, 5.21 ± 0.01, 5.59 ± 0.01, and 2.53 ± 0.01 mol m^{-2} $hour^{-1}$, respectively. The results clearly show that 1) compared with bare porous PTFE support, GO membranes with well-defined nanoscale 2D channels can efficiently slow down the permeation rate; 2) compared with pristine GO membrane, Mg-GO and Ca-GO did not show obvious decrease in the trans-membrane permeation rates, while Cu-GO membrane is more effective in blocking the transport of NaCl.

The transports of water and ions across the GO-based membranes are mainly determined by two factors, namely the size exclusion effect and charge effect (Fornasiero et al., 2008; Wang et al., 2017). It is worth noting that even though Mg-GO and Ca-GO have larger interlayer spacings in the wet state than pristine GO as detected in XRD patterns, their permeation rates change slightly. It can be thus inferred that the Mg^{2+} and Ca^{2+} might help enhance the local charge density in GO membrane, which to some extent offset the enlarged interlayer spacing therein. Likewise, the decreased permeation rate of Cu-GO can be ascribed to the synergistically enhanced size exclusion effect and charge effect.

Besides examining the trans-membrane permeation rates, reverse osmosis (RO) tests, widely used desalination technology where a strong external pressure is applied to overcome the osmotic pressure, were also carried out to interrogate the roles of divalent metal cations in GO as desalination membrane, as illustrated in Figure 5A. The rejection rate is defined as the concentration difference between the effluent and feed solution. Following previous works (Morelos-Gomez et al., 2017; Tan et al., 2018), Na_2SO_4 and NaCl solution with concentration of 1000 and 2000 ppm were used as feed solution. In such concentration regime where Kohlrausch's law stands, the rejection rate therefore can be calculated directly by the conductivity difference between the effluent and feed solution.

The results of RO tests are shown in Figures 5B–5E. It is unambiguously clear that the different roles of divalent metal cations in GO membrane during reverse osmosis test are also prominent. As compared with pristine GO membrane, Mg-GO and Ca-GO membrane have quite similar rejection rate and permeated water flux as well. However, Cu-GO membrane has an enhanced rejection rate and lowered permeated water flux. For instance, when using 1000 ppm NaCl feed solution, the rejection rates of GO, Mg-GO, Ca-GO, and Cu-GO are 70.9 ± 1.0 %, 69.2 ± 0.9 %, 72.5 ± 1.3 %, and 78.4 ± 0.6 %, with corresponding permeated water fluxes 0.15 ± 0.02, 0.14 ± 0.01, 0.12 ± 0.01, and 0.05 ± 0.01 liter per square meter per hour per bar (LMHB), respectively (Figure 5B). Clearly, Cu^{2+} modifications could lead to enhanced salt rejection rate and decreased water flux of GO membrane, while Mg^{2+} and Ca^{2+} modifications could not. Increasing the concentration of the feed solution leads to decreased salt rejection rate, as expected. However, the conclusion

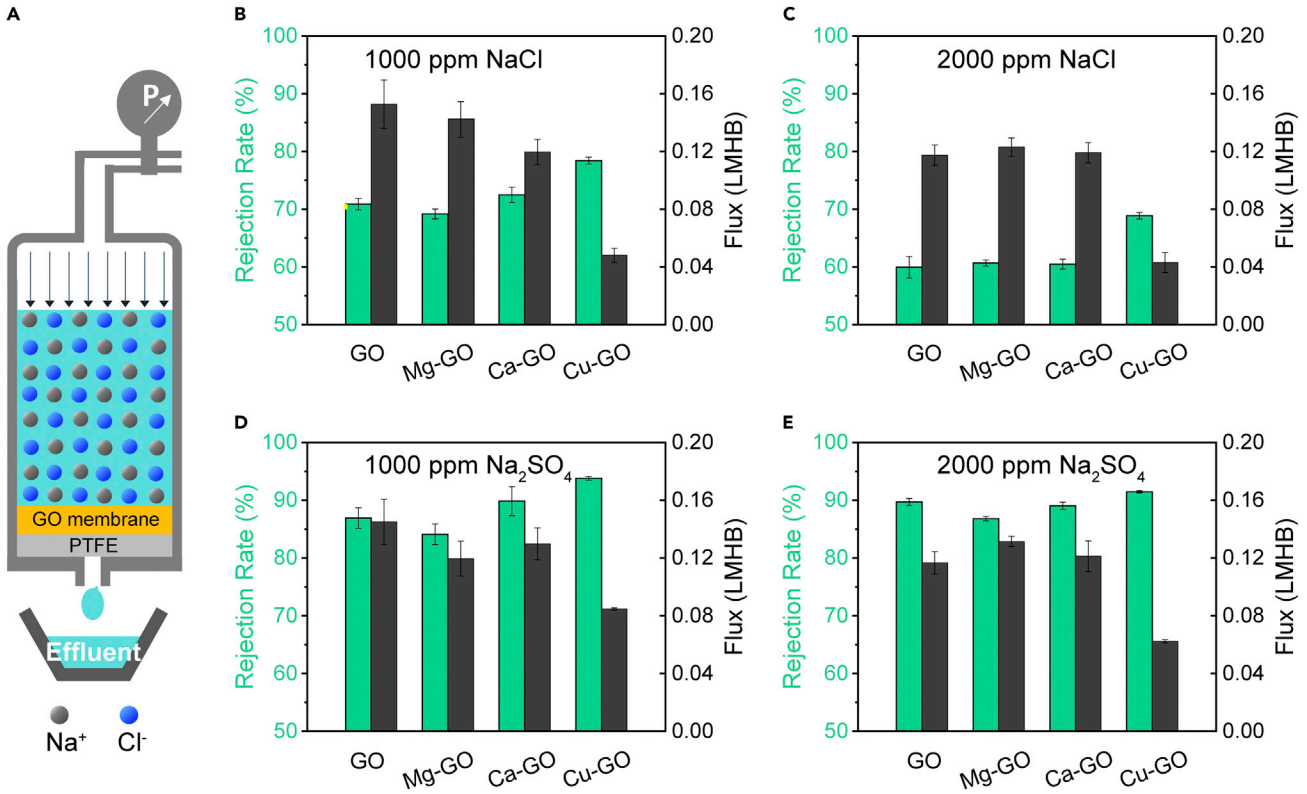

Figure 5. Reverse osmosis test

(A) Schematic of the reverse osmosis test.

(B–E) The performances of membranes using 1000 ppm NaCl (B), 2000 ppm NaCl (C), 1000 ppm Na_2SO_4 (D), and 2000 ppm Na_2SO_4 (E) as feed solution in reverse osmosis tests. The applied pressure was 15 bar.

of enhanced salt rejection rate and decreased water flux of GO membrane with Cu^{2+} modifications is still valid. For instance, when the 2000 ppm NaCl solution was used as feed, as shown in Figure 5C, the rejection rates of GO, Mg-GO, Ca-GO, and Cu-GO are 60.0±1.9 %, 60.7±0.6 %, 60.5±0.9 %, and 68.9±0.6 %, with corresponding permeated water fluxes 0.12±0.01, 0.12±0.01, 0.12±0.01, and 0.04±0.01 LMHB, respectively. Tests using Na_2SO_4 feed solution showed coherent trend. When using 1000 ppm Na_2SO_4 feed solution, the rejection rates of GO, Mg-GO, Ca-GO, and Cu-GO are 86.9±1.8%, 84.1±1.8 %, 89.8±2.5 %, and 93.8±0.3 %, with corresponding water fluxes 0.15±0.02, 0.12±0.01, 0.13±0.01, and 0.08±0.01 LMHB, respectively (Figure 5D). When the Na_2SO_4 feed concentration was elevated to 2000 ppm, the rejection rates of GO, Mg-GO, Ca-GO, and Cu-GO are 89.7±0.6 %, 86.8±0.4 %, 89.0±0.6 %, and 91.5±0.2%, with corresponding permeated water fluxes 0.12±0.01, 0.13±0.01, 0.12±0.01, and 0.06±0.01 LMHB, respectively (Figure 5E). Owing to the fact that sulfate anion is larger than chloride anion in size, as well as having large electrostatic repulsion effect, it is no surprise that all membranes showed higher rejection rates to Na_2SO_4 than to NaCl. All the results of reverse osmosis tests are consistent with the trans-membrane permeation rate results in Figure 4. No obvious change of flux and rejection rate was observed for Cu-GO membrane within the sampling duration (Figure S10). Our systematic tests coherently demonstrate the enhanced salt rejection of GO membrane with single-site Cu^{2+} modification, while Mg^{2+} and Ca^{2+} play a trivial part in GO as desalination membrane. The performance contrast of M-GO membranes in RO should be traced backed to the different water and ions configurations within the two-dimensional channel of GO membrane.

Conclusions

To conclude, we explored the roles of single-site divalent metal cations in tuning the interlayer chemistry of graphene oxide membrane and their influence on the mass transport through membrane. Our results reveal the exotic role of Cu^{2+} in graphene oxide membrane due to the strong interactions between graphene oxide matrices and single site Cu^{2+} cations. These strong interactions between Cu^{2+} and graphene

oxide matrices can suppress the swelling of graphene oxide membrane in the wet state, thus enabling a narrower interlayer spacing. With single-site Cu^{2+} modifications, graphene oxide membrane is endowed with enhanced salt rejection accordingly. By comparison, Mg^{2+} and Ca^{2+} did not show much effect in tuning the salt rejection of graphene oxide membrane.

Limitations of the study

This work demonstrates the control of ion transport in GO membranes via cation modification. Cu^{2+} decorates the GO membrane as single-site cations and is more effective in restricting the swelling of GO membranes comparing to other cations. A better membrane assembly process needs to be developed to decrease the membrane thickness and increase the flux to the level comparable to commercial polymeric membranes.

STAR★METHODS

Detailed methods are provided in the online version of this paper and include the following:

- KEY RESOURCES TABLE
- RESOURCE AVAILABILITY
  - Lead contact
  - Materials availability
  - Data and code availability
- EXPERIMENTAL MODEL AND SUBJECT DETAILS
- METHOD DETAILS
  - Materials
  - Membrane fabrication
  - Characterization
  - Competitive M^{2+} trans-membrane permeation test
  - Salt rejection tests of membrane
- QUANTIFICATION AND STATISTICAL ANALYSIS
- ADDITIONAL RESOURCES

SUPPLEMENTAL INFORMATION

Supplemental information can be found online at https://doi.org/10.1016/j.isci.2022.104044.

ACKNOWLEDGMENTS

This work is supported by the Pritzker School of Molecular Engineering and the Advanced Materials for Energy-Water-Systems (AMEWS) Center, an Energy Frontier Research Center funded by the U.S. Department of Energy, Office of Science, Basic Energy Sciences. We acknowledge helpful discussions with Nicholas H. C. Lewis. We acknowledge Electron Microscopy Core of Research Resources Center in University of Illinois at Chicago for TEM characterization. This research used resources of the Advanced Photon Source, a U.S. Department of Energy (DOE) Office of Science User Facility, operated for the DOE Office of Science by Argonne National Laboratory under Contract No. DE-AC02-06CH11357. Extraordinary facility operations were supported in part by the DOE Office of Science through the National Virtual Biotechnology Laboratory, a consortium of DOE national laboratories focused on the response to COVID-19, with funding provided by the Coronavirus CARES Act.

AUTHOR CONTRIBUTIONS

C. L. and M. W. designed the project. M. W. did the membrane fabrications, modifications, characterizations, and salt rejection tests. X.H. and D.M.T. performed the high-energy X-ray scattering measurements with the pair distribution function analysis. E.H. G.P. J.R. helped with materials preparations and data collections. G.Y. and G.H. helped with ICP-MS tests. F. S. did the TEM characterizations. H.Z. did the synchrotron-based X-ray absorption characterizations. M.W. and C.L. wrote up the manuscript. All the authors discussed the manuscript.

DECLARATION OF INTERESTS

The authors declare no competing financial interests.

Received: November 12, 2021
Revised: February 15, 2022
Accepted: March 8, 2022
Published: April 15, 2022

REFERENCES

Abraham, J., Vasu, K.S., Williams, C.D., Gopinadhan, K., Su, Y., Cherian, C.T., Dix, J., Prestat, E., Haigh, S.J., Grigorieva, I.V., et al. (2017). Tunable sieving of ions using graphene oxide membranes. Nat. Nanotechnol. *12*, 546–550.

Algara-Siller, G., Lehtinen, O., Wang, F.C., Nair, R.R., Kaiser, U., Wu, H.A., Geim, A.K., and Grigorieva, I.V. (2015). Square ice in graphene nanocapillaries. Nature *519*, 443–445.

Burgess, J. (1978). Metal Ions in Solution (Ellis Horwood), pp. 182–183.

Chen, L., Shi, G.S., Shen, J., Peng, B.Q., Zhang, B.W., Wang, Y.Z., Bian, F.G., Wang, J.J., Li, D.Y., Qian, Z., et al. (2017). Ion sieving in graphene oxide membranes via cationic control of interlayer spacing. Nature *550*, 415–418.

Chmiola, J., Yushin, G., Gogotsi, Y., Portet, C., Simon, P., and Taberna, P.L. (2006). Anomalous increase in carbon capacitance at pore sizes less than 1 nanometer. Science *313*, 1760–1763.

Cohen-Tanugi, D., and Grossman, J.C. (2012). Water desalination across nanoporous graphene. Nano Lett. *12*, 3602–3608.

Ding, L., Li, L.B., Liu, Y.C., Wu, Y., Lu, Z., Deng, J.J., Wei, Y.Y., Caro, J., and Wang, H.H. (2020). Effective ion sieving with Ti3C2Tx MXene membranes for production of drinking water from seawater. Nat. Sustain. *3*, 296–302.

Dreyer, D.R., Park, S., Bielawski, C.W., and Ruoff, R.S. (2010). The chemistry of graphene oxide. Chem. Soc. Rev. *39*, 228–240.

Elimelech, M., and Phillip, W.A. (2011). The future of seawater desalination: energy, technology, and the environment. Science *333*, 712–717.

Fang, Z.Y., Zhen, Y.R., Neumann, O., Polman, A., de Abajo, F.J.G., Nordlander, P., and Halas, N.J. (2013). Evolution of light-induced vapor generation at a liquid-immersed metallic nanoparticle. Nano. Lett. *13*, 1736–1742.

Fievet, P. (2014). Donnan effect. In Encyclopedia of Membranes, E. Drioli and L. Giorno, eds. (Springer), pp. 572–574.

Fornasiero, F., Park, H.G., Holt, J.K., Stadermann, M., Grigoropoulos, C.P., Noy, A., and Bakajin, O. (2008). Ion exclusion by sub-2-nm carbon nanotube pores. Proc. Natl. Acad. Sci. U S A. *105*, 17250–17255.

Holt, J.K., Park, H.G., Wang, Y.M., Stadermann, M., Artyukhin, A.B., Grigoropoulos, C.P., Noy, A., and Bakajin, O. (2006). Fast mass transport through sub-2-nanometer carbon nanotubes. Science *312*, 1034–1037.

Huang, L., Zhang, M., Li, C., and Shi, G.Q. (2015). Graphene-based membranes for molecular separation. J. Phys. Chem. Lett. *6*, 2806–2815.

Humplik, T., Lee, J., O'Hern, S.C., Fellman, B.A., Baig, M.A., Hassan, S.F., Atieh, M.A., Rahman, F., Laoui, T., Karnik, R., et al. (2011). Nanostructured materials for water desalination. Nanotechnology *22*, 292001.

Jia, C., Li, Y.J., Yang, Z., Chen, G., Yao, Y.G., Jiang, F., Kuang, Y.D., Pastel, G., Xie, H., Yang, B., et al. (2017). Rich mesostructures derived from natural woods for solar steam generation. Joule *1*, 588–599.

Jia, Z.Q., Wang, Y., Shi, W.X., and Wang, J.L. (2016). Diamines cross-linked graphene oxide free-standing membranes for ion dialysis separation. J. Membr. Sci. *520*, 139–144.

Joshi, R.K., Carbone, P., Wang, F.C., Kravets, V.G., Su, Y., Grigorieva, I.V., Wu, H.A., Geim, A.K., and Nair, R.R. (2014). Precise and ultrafast molecular sieving through graphene oxide membranes. Science *343*, 752–754.

Juhás, P., Davis, T., Farrow, C.L., and Billinge, S.J. (2013). PDFgetX3: a rapid and highly automatable program for processing powder diffraction data into total scattering pair distribution functions. J. Appl. Crystallogr. *46*, 560–566.

Liu, J., Shi, G.S., Guo, P., Yang, J.R., and Fang, H.P. (2015). Blockage of water flow in carbon nanotubes by ions due to interactions between cations and aromatic rings. Phys. Rev. Lett. *115*, 6.

Lv, X.B., Xie, R., Ji, J.Y., Liu, Z., Wen, X.Y., Liu, L.Y., Hu, J.Q., Ju, X.J., Wang, W., and Chu, L.Y. (2020). A novel strategy to fabricate cation-cross-linked graphene oxide membrane with high aqueous stability and high separation performance. Acs Appl. Mater. Inter. *12*, 56269–56280.

Mahadevi, A.S., and Sastry, G.N. (2013). Cation-π interaction: its role and relevance in chemistry, biology, and material science. Chem. Rev. *113*, 2100–2138.

Mathesh, M., Liu, J.Q., Nam, N.D., Lam, S.K.H., Zheng, R.K., Barrow, C.J., and Yang, W.R. (2013). Facile synthesis of graphene oxide hybrids bridged by copper ions for increased conductivity. J. Mater. Chem. C. *1*, 3084–3090.

Mi, B.X. (2019). Scaling up nanoporous graphene membranesc. Science *364*, 1033–1034.

Morelos-Gomez, A., Cruz-Silva, R., Muramatsu, H., Ortiz-Medina, J., Araki, T., Fukuyo, T., Tejima, S., Takeuchi, K., Hayashi, T., Terrones, M., et al. (2017). Effective NaCl and dye rejection of hybrid graphene oxide/graphene layered membranes. Nat. Nanotechnol. *12*, 1083–1088.

Nair, R.R., Wu, H.A., Jayaram, P.N., Grigorieva, I.V., and Geim, A.K. (2012). Unimpeded permeation of water through helium-leak-tight graphene-based membranes. Science *335*, 442–444.

Nie, L., Goh, K., Wang, Y., Lee, J., Huang, Y.J., Karahan, H.E., Zhou, K., Guiver, M.D., and Bae, T.H. (2020). Realizing small-flake graphene oxide membranes for ultrafast size-dependent organic solvent nanofiltration. Sci. Adv. *6*, eaaz9184.

Nightingale, E.R. (1959). Phenomenological theory of ion solvation - effective radii of hydrated ions. J. Phys. Chem. *63*, 1381–1387.

O'Hern, S.C., Jang, D., Bose, S., Idrobo, J.C., Song, Y., Laoui, T., Kong, J., and Karnik, R. (2015). Nanofiltration across defect-sealed nanoporous monolayer graphene. Nano Lett. *15*, 3254–3260.

Ohkubo, T., Gin, S., Collin, M., and Iwadate, Y. (2018). Molecular dynamics simulation of water confinement in disordered aluminosilicate subnanopores. Sci. Rep. *8*, 3761.

Park, H.B., Kamcev, J., Robeson, L.M., Elimelech, M., and Freeman, B.D. (2017). Maximizing the right stuff: the trade-off between membrane permeability and selectivity. Science *356*, eaab0530.

Park, S., Lee, K.-S., Bozoklu, G., Cai, W., Nguyen, S.T., and Ruoff, R.S. (2008). Graphene oxide papers modified by divalent ions - enhancing mechanical properties via chemical cross-linking. ACS Nano. *2*, 572–578.

Shannon, M.A., Bohn, P.W., Elimelech, M., Georgiadis, J.G., Marinas, B.J., and Mayes, A.M. (2008). Science and technology for water purification in the coming decades. Nature *452*, 301–310.

Shi, G.S., Liu, J., Wang, C.L., Song, B., Tu, Y.S., Hu, J., and Fang, H.P. (2013). Ion enrichment on the hydrophobic carbon-based surface in aqueous salt solutions due to cation-π interactions. Sci. Rep. *3*, 3436.

Sun, P.Z., Wang, K.L., and Zhu, H.W. (2016). Recent developments in graphene-based membranes: structure, mass-transport mechanism and potential applications. Adv. Mater. *28*, 2287–2310.

Sun, P.Z., Zheng, F., Zhu, M., Song, Z.G., Wang, K.L., Zhong, M.L., Wu, D.H., Little, R.B., Xu, Z.P., and Zhu, H.W. (2014). Selective trans-membrane transport of alkali and alkaline earth cations through graphene oxide membranes based on cation-π interactions. ACS Nano. *8*, 850–859.

Sun, S.A., Wang, C.Y., Chen, M.M., and Li, M.W. (2013). The mechanism for the stability of graphene oxide membranes in a sodium sulfate solution. Chem. Phys. Lett. *561*, 166–169.

Surwade, S.P., Smirnov, S.N., Vlassiouk, I.V., Unocic, R.R., Veith, G.M., Dai, S., and Mahurin, S.M. (2015). Water desalination using nanoporous single-layer graphene. Nat. Nanotechnol. *10*, 459–464.

Tan, P., Hu, Y.Y., and Bi, Q. (2016). Competitive adsorption of Cu2+, Cd2+ and Ni2+ from an aqueous solution on graphene oxide membranes. Colloid Surf. A Physicochem. Eng. Asp. *509*, 56–64.

Tan, Z., Chen, S.F., Peng, X.S., Zhang, L., and Gao, C.J. (2018). Polyamide membranes with nanoscale Turing structures for water purification. Science *360*, 518–521.

Thebo, K.H., Qian, X.T., Zhang, Q., Chen, L., Cheng, H.M., and Ren, W.C. (2018). Highly stable graphene-oxide-based membranes with superior permeability. Nat. Commun. *9*, 1486.

Wang, E.N., and Karnik, R. (2012). Graphene cleans up water. Nat. Nanotechnol. *7*, 552–554.

Wang, L.D., Boutilier, M.S.H., Kidambi, P.R., Jang, D., Hadjiconstantinou, N.G., and Karnik, R. (2017). Fundamental transport mechanisms, fabrication and potential applications of nanoporous atomically thin membranes. Nat. Nanotechnol. *12*, 509–522.

Wang, Z.Z., Ma, C., Xu, C.Y., Sinquefield, S.A., Shofner, M.L., and Nair, S. (2021). Graphene oxide nanofiltration membranes for desalination under realistic conditions. Nat. Sustain. *4*, 402–408.

Werber, J.R., Osuji, C.O., and Elimelech, M. (2016). Materials for next-generation desalination and water purification membranes. Nat. Rev. Mater. *1*, 16018.

Woznica, N., Hawelek, L., Fischer, H.E., Bobrinetskiy, I., and Burian, A. (2015). The atomic scale structure of graphene powder studied by neutron and X-ray diffraction. J. Appl. Crystallogr. *48*, 1429–1436.

Yang, H.C., Chen, Z.W., Xie, Y.S., Wang, J., Elam, J.W., Li, W.H., and Darling, S.B. (2019a). Chinese ink: a powerful photothermal material for solar steam generation. Adv. Mater. Inter. *6*, 1801252.

Yang, Y.B., Yang, X.D., Liang, L., Gao, Y.Y., Cheng, H.Y., Li, X.M., Zou, M.C., Cao, A.Y., Ma, R.Z., Yuan, Q., et al. (2019b). Large-area graphene-nanomesh/carbon-nanotube hybrid membranes for ionic and molecular nanofiltration. Science *364*, 1057–1062.

Yeh, C.N., Raidongia, K., Shao, J.J., Yang, Q.H., and Huang, J.X. (2015). On the origin of the stability of graphene oxide membranes in water. Nat. Chem. *7*, 166–170.

Zhang, Q., Qian, X.T., Thebo, K.H., Cheng, H.M., and Ren, W.C. (2018). Controlling reduction degree of graphene oxide membranes for improved water permeance. Sci. Bull. *63*, 788–794.

Zhao, F., Zhou, X.Y., Shi, Y., Qian, X., Alexander, M., Zhao, X.P., Mendez, S., Yang, R.G., Qu, L.T., and Yu, G.H. (2018). Highly efficient solar vapour generation via hierarchically nanostructured gels. Nat. Nanotechnol. *13*, 489–495.

Zhou, L., Tan, Y.L., Wang, J.Y., Xu, W.C., Yuan, Y., Cai, W.S., Zhu, S.N., and Zhu, J. (2016). 3D self-assembly of aluminium nanoparticles for plasmon-enhanced solar desalination. Nat. Photon. *10*, 393–398.

STAR★METHODS

KEY RESOURCES TABLE

REAGENT or RESOURCE	SOURCE	IDENTIFIER
Chemicals and reagents		
$MgCl_2$ (anhydrous, 99%)	Alfa Aesar	CAT# AA12315A1
$CuCl_2.2H_2O$ (99+%)	Acros Organics	CAT# AC315281000
$CaCl_2{\cdot}2H_2O$ (99%)	Sigma Aldrich	Product No: 31307
NaCl (99.5+%)	Sigma Aldrich	Product No: S7653
Na_2SO_4 (>99%)	Sigma Aldrich	Product No: 746363
copper acetate hydrate (98%)	Sigma Aldrich	Product No: 341746
Omnipore™ PTFE support (0.2 um, hydrophilic)	Sigma Aldrich	Part No: JGWP04700
Graphene oxide	SHENZHEN DX TIME TECHNOLOGY Co. LTD	Large sheet GO slurry

RESOURCE AVAILABILITY

Lead contact

Further information and requests for resources and reagents should be directed to and will be fulfilled by the lead contact, Prof. Chong Liu (chongliu@uchicago.edu).

Materials availability

This study did not generate new unique reagents

Data and code availability

- All data reported in this paper will be shared by the lead contact upon request.
- No new code was generated. This is an experimental study of the sieving effect of graphene oxide membrane.
- Any additional information required to reanalyze the data reported in this paper is available from the lead contact upon request.

EXPERIMENTAL MODEL AND SUBJECT DETAILS

The graphene oxide (GO) membranes were prepared through vacuum-assisted filtration method. The divalent cation modifications were made. Then as-prepared divalent ions modified GO membranes were used for structural characterizations, permeation tests and reverse osmosis tests.

METHOD DETAILS

Materials

Omnipore™ PTFE support (0.2 um) was purchased from Sigma Aldrich. $MgCl_2$ (anhydrous, 99%) was purchased from Alfa Aesar. $CuCl_2.2H_2O$ (99+%) was purchased from Acros Organics. $CaCl_2{\cdot}2H_2O$ (99%), NaCl (99.5+%), Na_2SO_4 (>99%) and copper acetate hydrate (98%) were purchased from Sigma Aldrich. All these chemicals were used as received without further treatment.

Membrane fabrication

Graphene oxide (GO) solution (~0.5 mg mL^{-1}) was diluted from GO slurries (which were purchased from SHENZHEN DX TIME TECHNOLOGY Co. LTD). The GO solution was thoroughly dialyzed to remove residual ions and other impurities before membrane fabrication.

For the pristine GO membrane fabrication, 1 mL dialyzed GO solution was diluted into ~20 mL with DI water. Then the diluted solution was filtered onto porous PTFE support under the assistance of vacuum. For

the divalent metal cation modified GO membrane, corresponding solution (5 mL, 0.01M $MgCl_2$, $CaCl_2$ and $CuCl_2$) was then filtered onto as-prepared pristine GO membrane. Then the membrane was thoroughly washed with DI water until the conductivity of washing water was <10 μS/cm. Finally, the as-prepared wet GO membranes were transferred onto Petri dishes and left dry naturally for further tests.

Characterization

HAADF-STEM images were taken on JEOL JEM-ARM200CF under 80 kV. AFM was done on Bruker 3A/MultiMode 5. SEM was done on Carl Zeiss Merlin. Raman spectra were collected on Horiba LabRAM HR Evolution. UV-Vis spectra were collected on Shimadzu UV-3600 Plus UV-VIS-NIR Dual Beam Spectrophotometer. XPS was tested on KRATOS AXIS NOVA X-ray Photoelectron Spectrometer. XRD patterns were performed on Bruker D8 Powder X-ray Diffractometer. ICP-MS data were collected on Thermo iCapQ ICP-MS equipped with collision cell technology. Synchrotron-based X-ray absorption spectra (e.g., X-ray absorption near edge structure (XANES) and extended X-ray absorption fine structure (EXAFS) measurements) were collected at the beamline 12-BM of Advanced Photon Source (APS) at Argonne National Laboratory. The XANES and EXAFS spectra were taken under ambient temperature at the absorption K-edge of Cu. The acquired XANES and EXAFS data were processed according to standard procedures using the ATHENA software. The high-energy X-ray scattering (HEXS) with pair distribution function (PDF) analysis was performed at 11-ID-B of APS at Argonne National Laboratory, where the data collection was conducted under ambient conditions with the synchrotron radiation (58.7 keV). The Kapton film and CeO_2 powder were used as the sample background and standard for detector alignment, respectively. The integration of the raw scattering images into the Q-space diffraction data was carried out in GSAS-II, which were then converted to the reduced structure functions and real-space PDF patterns following standard PDFGetX3 procedure(Juhás et al., 2013).

Competitive M^{2+} trans-membrane permeation test

In the trans-membrane test of Figure 2, solutions in the permeate and the feed were continuously sampled out during the permeation test for ICP-MS test to check the concentrations of the metal cations. During the permeation test, both chambers were tightly sealed to avoid concentration change due to water evaporation. The test was done at ~ 20°C. The *p*H value of the mixture solution was ~4.7.

Salt rejection tests of membrane

The conductivity measurements were performed on Seven Excellence *p*H/Ion/Cond meter S475 and Orion Star. Reverse osmosis tests were done using Sterlitech HP4750 High Pressure Stirred Cell. At least three membranes were tested for each kind of membrane. The tests were done at ~ 20°C. The *p*H values of the feed salt solution were ~5.3–5.7.

QUANTIFICATION AND STATISTICAL ANALYSIS

The conductivities of relevant solutions were collected on Seven Excellence pH/Ion/Cond meter S475 and Orion Star. The concentrations of metal cations were measured through ICP-MS tests on Thermo iCapQ ICP-MS equipped with collision cell technology. Figures are produced in Origin from the raw data.

ADDITIONAL RESOURCES

Any additional information about the graphene oxide membrane fabrication, permeation tests, reverse osmosis test and data reported in this paper is available from the lead contact on request.